# Quantitative Analysis of 1300-nm Three-photon Calcium Imaging in the Mouse Brain

Tianyu Wang[1†*], Chunyan Wu[1,5†], Dimitre G. Ouzounov[1], Wenchao Gu[2], Fei Xia[3], Minsu Kim[4], Xusan Yang[1], Melissa R. Warden[2], and Chris Xu[1*]

[1]School of Applied and Engineering Physics, Cornell University, Ithaca, New York, USA.

[2]Department of Neurobiology and Behavior, Cornell University, Ithaca, New York, USA.

[3]Meining School of Biomedical Engineering, Cornell University, Ithaca, New York, USA.

[4]College of Human Ecology, Cornell University, Ithaca, New York, USA

[5]College of Veterinary Medicine, Cornell University, Ithaca, New York, USA

[†] T.W and C. W. contributed equally to this work.

Corresponding authors:

Email: tw329@cornell.edu and cx10@cornell.edu

## Abstract (150 words limit)

1300-nm three-photon calcium imaging has emerged as a useful technique to allow calcium imaging in deep brain regions. Application to large-scale neural activity imaging entails a careful balance between recording fidelity and tissue heating. We calculated and experimentally verified the excitation pulse energy to achieve *the minimum photon count* required for the detection of calcium transients in GCaMP6s-expressing neurons for 920-nm two-photon and 1320-nm three-photon excitation, respectively. Brain tissue heating by continuous three-photon imaging was simulated with Monte Carlo method and experimentally validated with immunohistochemistry. We observed increased immunoreactivity with 150 mW excitation power at 1.0- and 1.2-mm imaging depths. Based on the data, we explained how three-photon excitation achieves better calcium imaging fidelity than two-photon excitation in the deep brain and quantified the imaging depth where three-photon microscopy should be applied. Our analysis presents a translatable model for the optimization of three-photon calcium imaging based on experimentally tractable parameters.

## Introduction

Multiphoton microscopy (MPM) combined with genetically encoded calcium indicators (GECIs) is a powerful functional imaging technique widely applied to *in vivo* neurophysiological recordings (Lin and Schnitzer, 2016; Yang and Yuste, 2017). In the mouse brain, 2-photon microscopy (2PM) has enabled activity recording from thousands of neurons with single-cell resolution (Sofroniew et al., 2016; Stirman et al., 2016; Weisenburger et al., 2019). Although 2-photon excitation (2PE) can effectively reduce out-of-focus fluorescence, the background intensity eventually becomes comparable to the signal in non-sparsely labeled samples, as the excitation power grows exponentially with imaging depth. The background not only reduces image contrast but also introduces additional noise inseparable from the true calcium transient signal, which irreversibly reduces imaging quality. In the mouse neocortex, 2PM signal-to-background ration (SBR) decreases to 1 at ~4.7 attenuation lengths with a labeling density of ~ 2% (Kobat et al., 2011; Theer et al., 2003; Theer and Denk, 2006)

3-photon microscopy (3PM) has emerged as a useful tool for imaging in deep brain regions that are typically inaccessible to 2PM. Although deep calcium imaging with 2PM has been demonstrated with red-shifted calcium indicators using 1100 nm excitation, these methods suffer from limitations such as staining only a single layer of the cortical neurons (Tischbirek et al., 2015), or in the hippocampus of young mice less than 6 weeks old (Inoue et al., 2019; Kondo et al., 2017). Furthermore, the best red-shifted GECIs are currently less bright and robust than their green counterparts (e.g., < 40% the cross section of GCaMP6s and < 50% sensitivity of jGCaMP7 (Dana et al., 2019, 2016)), which further limits their application to large-scale recordings. Compared to the red GECIs, the shorter 2PE wavelength (900-960 nm) for GCaMP results in more tissue scattering

(Jacques, 2013). Consequently, 2-photon imaging with GCaMP faces more technical challenges in the deep brain, and usually requires the removal of the superficial cortex or the insertion of penetrating optical elements (Attardo et al., 2015; Dombeck et al., 2010; Low et al., 2014; Pilz et al., 2016). In comparison, 1300-nm 3PM has enabled activity imaging with GCaMP6 of the entire densely labeled cortex (Takasaki et al., 2019b; Yildirim et al., 2019) and the hippocampus in intact *adult* mouse brains (8-16 weeks old) (Ouzounov et al., 2017; Takasaki et al., 2019a; Weisenburger et al., 2019), because of the background suppression by 3-photon excitation (3PE) and the reduced tissue attenuation by the longer excitation wavelength (Ouzounov et al., 2017).

Since the first demonstrations of 3PM for *in vivo* brain imaging (Horton et al., 2013; Ouzounov et al., 2017), a number of research groups have successfully adopted and developed the technology (Chen et al., 2018; Escobet-Montalbán et al., 2018; Odríguez, 2018; Perillo et al., 2017; Rowlands et al., 2017; Takasaki et al., 2019b; Weisenburger et al., 2019; Yildirim et al., 2019), propelled by the commercially available lasers and microscopes. To facilitate 3PM applications, here we provide a quantitative characterization of three-photon deep-brain calcium imaging, with a side-by-side comparison to 2PM with 920 nm excitation. Our results show that 1320-nm 3PM is advantageous in terms of both signal strength and imaging contrast in the deep cortex and beyond. Furthermore, by optimizing the important imaging parameters (e.g., pulse energy and repetition rate) to meet the signal-to-noise ratio within the power constraints, we provide a scalable strategy to push the limits of 3PM for large penetration depth and field-of-view (FOV).

## Results

### Photon count provides the fundamental metric for calcium imaging quality.

High-quality calcium imaging enables reliable detection of calcium transients in the presence of noise. With a photomultiplier tube as the fluorescence detector, calcium imaging can be performed at the photon shot noise limit, where the photon fluctuation noise (N) and the signal (S) obey the relation: $N=S^{1/2}$. Therefore, quantifying the fluorescence signal with photon counts provides the noise statistics, and allows probabilistic inference of the true underlying signal. Assuming exponential decay of calcium transients, a single discriminability index (d'), as defined by equation (1), has been derived in the past to assess the recording fidelity of a calcium transient (Wilt et al., 2013):

$$d' \approx \frac{\Delta F}{F}\sqrt{\frac{F_0\tau}{2}} \quad (1)$$

where $\tau$ is the decay time, ΔF/F is the peak fluorescence change of a single-action-potential-induced calcium spike, and $F_0$ is the baseline brightness of the neuron. This expression holds as long as the frame rate is high enough to sample the exponential decay of the fluorescence intensity, and a higher d' value indicates better calcium transient detection accuracy. In fact, the fidelity of calcium imaging is determined by the signal photon counts of each neuron. The *minimum photon counts* required to detect a calcium transient induced by a single action potential can be calculated at any given confidence level: using the parameters for GCaMP6s (ΔF/F ~ 30% and $\tau$ ~ 2s) (Chen et al., 2013), $F_0$ is calculated to be ~100 photons/second to achieve d'=3, which allows 93% true detection and 7% false-positive detection rate. For large calcium transients induced by a short burst of multiple action potentials, $F_0$ can be significantly lower since ΔF/F is larger by the accumulation of single-action-potential ΔF/F (Wilt et al., 2013). Given ΔF/F and $\tau$ of a

calcium indicator are fixed, the quality of calcium imaging can only be improved by increasing the baseline neuron brightness $F_0$, which can be achieved by varying the imaging parameters, e.g., excitation repetition rate, pulse duration, pulse energy, focal spot size and laser dwell time on each neuron. It is clear from the above analysis that extremely high sampling rates in either pixel or frame do not improve the overall calcium transient detection accuracy since the number of photons per neuron per second is conserved regardless of the sampling scheme.

**1320-nm 3PE is more power-efficient in signal generation than 920-nm 2PE in the deep cortex and beyond.**

In general, due to the higher-order nonlinear excitation, 3PE requires higher excitation intensity at the focus in order to generate the same amount of fluorescence as 2PE. For deep tissue imaging, however, the pulse energy at the brain surface can be less for 3PE than 2PE because photons at the longer wavelength used for 3PE experience less attenuation. To quantify the difference in tissue attenuation caused by the wavelength, we imaged mouse brain vasculature uniformly labeled with fluorescein dextran and measured fluorescence signal decay as a function of depth. We centered the 3PE and 2PE excitation spectra at 1320 nm and 920 nm, respectively, since they are nearly optimal for GCaMP6 imaging, which is the focus of this study (Ouzounov et al., 2019). Through simultaneous 2PM and 3PM imaging of the same blood vessel with the same fluorescent label, we ensured the same signal collection efficiency for the two imaging modalities, and any sample fluctuation over time is eliminated. As shown in Figure 1A, the effective attenuation length (EAL) at 1320 nm in the mouse cortex is almost twice that at 920 nm (297±11 μm vs. 153±10 μm, mean ± standard deviation, n=4, >12 weeks old mice, all males, Figure 1A and Figure 1 - figure supplement 1).

We measured the pulse energy required for the typical multiphoton signal strength of 0.1 photons detected per excitation pulse (Figure 1B). To generate the same amount of signal in fluorescein-labeled blood vessels located at the brain surface, 3PE requires about 15 times the pulse energy of 2PE (1.1 ± 0.03 nJ vs. 0.07 ± 0.004 nJ, mean ± 95% confidence interval). As the imaging depth increases, to maintain the same signal strength, the 2PE pulse energy delivered to the brain surface has to increase more rapidly than that for 3PE since 920-nm photons experience more tissue attenuation than 1320-nm photons. Eventually, 3PE becomes more power-efficient than 2PE at a depth of around 750 µm, which is defined here as the cross-over depth. The same trend can be observed in GCaMP6s labeled neurons. At the brain surface, 3PE at 1320 nm requires ~ 8 times the pulse energy as 2PE at 920 nm (1.86 ± 0.27 nJ vs. 0.24 ± 0.05 nJ, mean ± 95% confidence interval), while in cortical layers at depth around 700 µm, the pulse energy required for 3PE becomes comparable to that of 2PE at the brain surface. The measured ratio of the 3PE to 2PE pulse energy and the cross-over depth are in good agreement with the calculation based on typical 2PE and 3PE cross sections (Appendix 1). Our data show that, with the same repetition rate and pulse duration, 3PM is more power-efficient than 2PM when imaging in the deep cortex and beyond. In other words, even if 2PM were used to image at the same depth (e.g., ~1 mm), its repetition rate will have to be reduced to the same level as 3PM (typically ~1 MHz) to avoid tissue heating by the average power. This result is consistent with previous studies on deep brain two-photon imaging, where the repetition rates were reduced to below 1 MHz at ~1 mm imaging depth (Theer et al., 2003; M. Wang et al., 2018). Although our data were measured with fluorescein and GCaMP6s, the conclusion is likely applicable to other green fluorescent dyes.

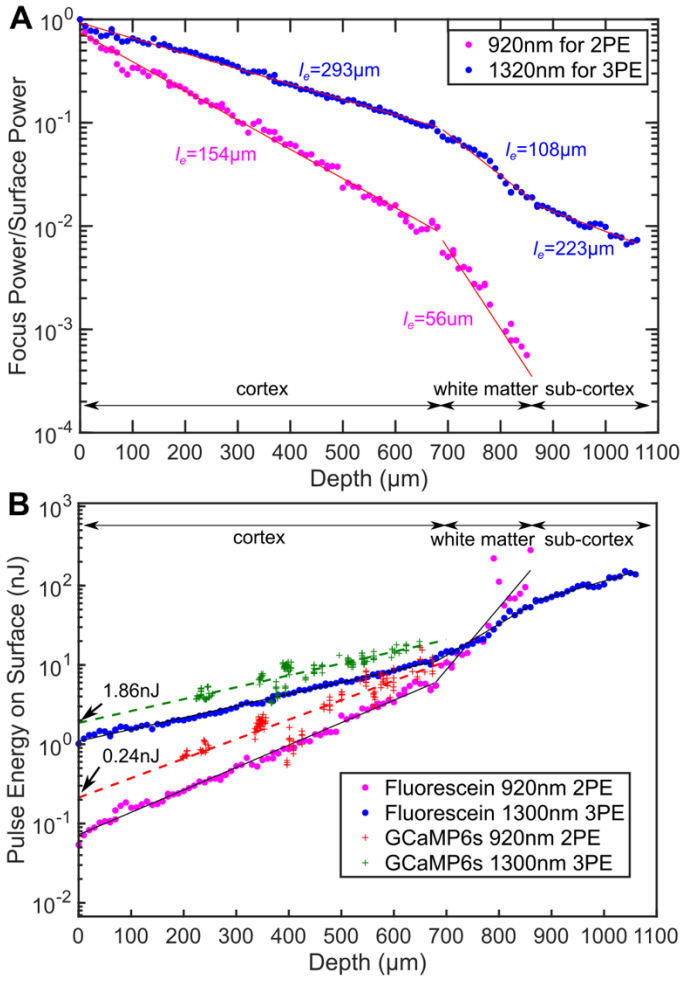


Figure 1. Comparison of the power attenuation of 1320-nm and 920-nm excitation lights and their respective 3-photon and 2-photon excitation efficiency in the mouse brain. (A) Power attenuation of 920-nm and 1320-nm excitation light in the mouse brain. The mouse brain vasculature was *uniformly* labeled with fluorescein dextran and imaged *simultaneously* by 920-nm 2PM and 1320-nm 3PM at precisely the same location. The fraction of excitation power reaching the focus from the brain surface (Focus Power/Surface Power) was calculated based on the attenuation of 2PE and 3PE signal with the imaging depth (Materials and Methods). (B) The pulse energy required at the brain surface to generate the *same* 2PE and 3PE signal strength (0.1 signal photons detected per laser pulse) at different imaging depths, measured in fluorescein-labeled blood vessels (n=1

shown) and GCaMP6s-labeled neurons (CamKII-tTA/tetO-GCaMP6s; n=5 mice). The signal strength is scaled to 60 fs pulse duration for both 2PE and 3PE.

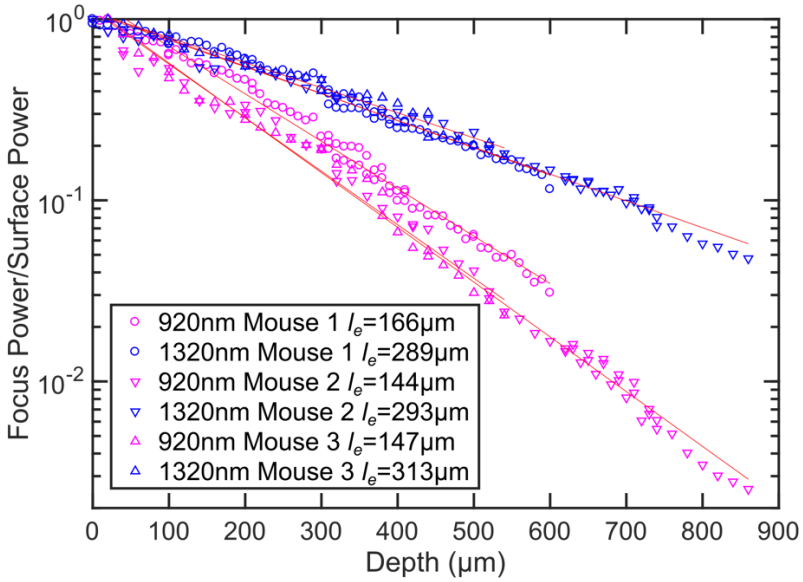


Figure 1 - figure supplement 1. Additional power attenuation curves of 920-nm and 1320-nm excitation light in the mouse neocortex (n=3, >12 weeks old mice, all males).

**1320-nm 3PM has orders of magnitude higher SBR than 920-nm 2PM for deep imaging in the non-sparsely labeled mouse brain.**

The imaging depth of 2PM is limited by the out-of-focus background in non-sparsely labeled samples (Theer and Denk, 2006). The SBR of an image is quantified as follows: the background is measured as the fluorescence intensity in structures not labeled, and the signal is the fluorescence signal within the labeled structures minus the background. For both 2PM and 3PM, the background is negligible at the sample surface, with SBR ~100 in fluorescein-labeled blood vessels (Figure 2A and Figure 2B). As the imaging depth increases beyond 600 μm in the cortex, 920-nm 2PM background starts to increase rapidly, accompanied by apparent degradation of image quality (Figure 2A and Figure 2C lower panel). Since the SBR of 2PM depends on the staining

density of the sample, we quantified the fractional vascular volume (2 ± 1%, mean ± standard deviation) and staining inhomogeneity (~50) of the labeled blood vessels (Figure 2-figure supplement 1 – Materials and Methods). According to the theoretical calculation, the SBR of 2PM reaches 1 at ~4.7 EALs at such a staining inhomogeneity (Theer and Denk, 2006), which is in close agreement with our *in vivo* measurement (Figure 2B). In contrast, 1320-nm 3PM does not show any increase in the background until in the white matter (Figure 2A and Figure 2B). The background reduction by 3PE was contributed by the larger EAL of the long wavelength that reduces the normalized imaging depth (z/EAL), and the higher order of nonlinearity of 3PE that suppresses background generation in the out-of-focus volume, which plays a critical role when the 2PE and 3PE used the same wavelength and have the same EAL (T. Wang et al., 2018). Large SBRs (> 40) were reported on 3-photon imaging of mouse brain vasculature at an imaging depth of greater than 5 attenuation lengths (Liu et al., 2019). However, for the depths beyond the white matter, our measured SBR of 3PM is lower than the theoretical prediction, which may be caused by the deterioration of the point spread function due to the strong aberration introduced by the white matter. Similar behavior was also observed in through-skull imaging (T. Wang et al., 2018).

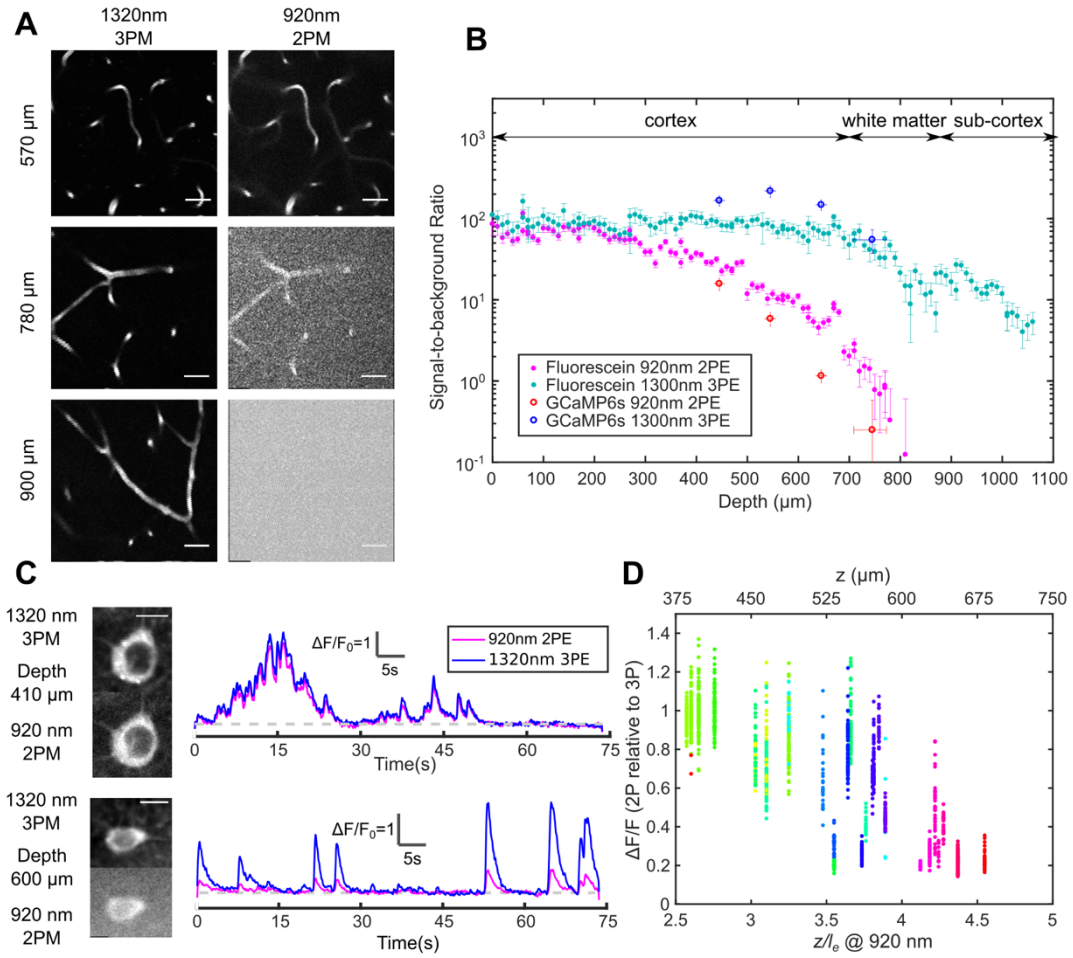


Figure 2. Comparison of signal-to-background ratio for 1320-nm 3PM and 920-nm 2PM in the non-sparsely labeled mouse brain and its effect on calcium imaging sensitivity. (A) Comparison of 3PM and 2PM images of fluorescein-labeled blood vessels at different depths. Scale bar 30 µm. (B) SBR measured *simultaneously* by 1320-nm 3PE and 920-nm 2PE on fluorescein-labeled blood vessels and GCaMP6s-labeled neurons, respectively. Each set of 3PE and 2PE comparison was performed in the same mouse. All vertical error bars denote the standard deviation of SBR caused by feature brightness variation, and horizontal error bars represent the depth range of the measurement. (C) Images and corresponding calcium traces of a cortical L4 neuron (410 µm) and a L5 neuron (600 µm), simultaneously recorded by 920-nm 2PM and 1320-nm 3PM. Both traces were low-pass filtered with a hamming window of a time constant 0.37 s. Scale bar, 10 µm. (D) The ratio of ΔF/F

calculated on simultaneously recorded 3PM and 2PM calcium traces (CamKII-tTA/tetO-GCaMP6s; n=3 mice). Each point was measured on a single calcium transient. The depth was normalized by the 2PM attenuation length at 920 nm of each animal to collapse the data better onto a single trendline. Data points from different neurons at the same depth are colored differently.

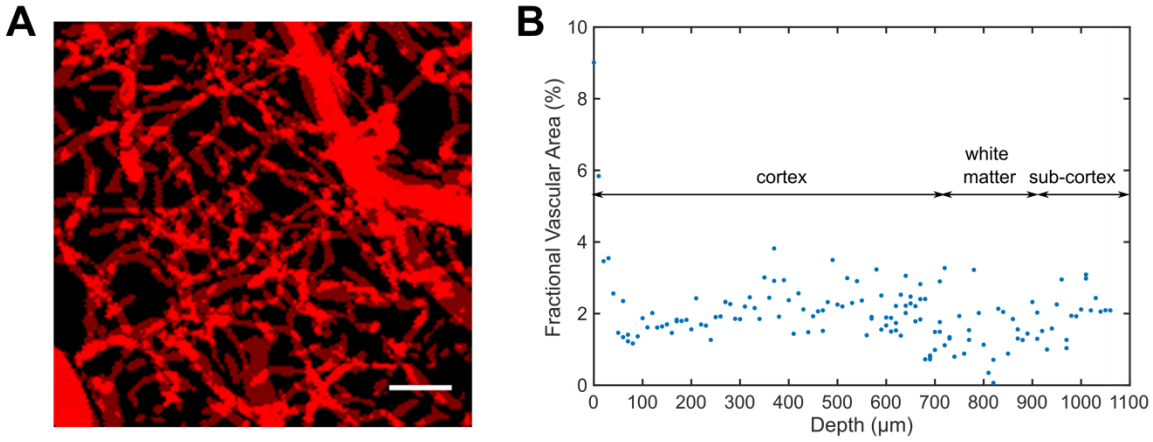


Figure 2-figure supplement 1. Measurement of the staining density in uniformly labeled vasculature.

(A) Z-projection of the identified blood vessels by summing all the XY-images in a vertical image stack (0-400 μm deep, with 10 μm step size). Scale bar, 30 μm.

(B) The fractional vascular area in each XY-image at various depths.

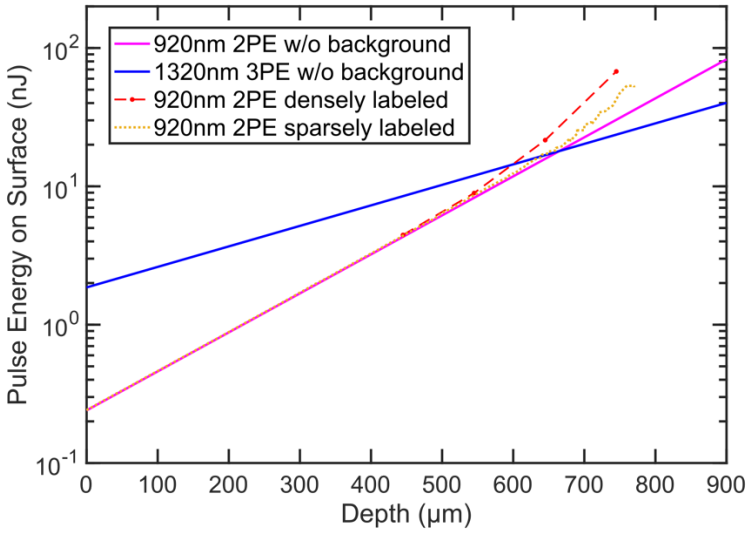


Figure 2-figure supplement 2. The pulse energy required at the brain surface to generate *the same d'* per pulse sampling the neuron for 2PE and 3PE of GCaMP6s at different imaging depths. In the

absence of the background fluorescence, d' is entirely determined by signal photon counts: when a neuron is sampled by 1000 excitation pulses in 1s, it generates $F_0 = 1000\ \text{pulses} \times 0.1\ \text{photons/pulse} = 100\ \text{photons/s}$, which gives $d' \sim 3$. Therefore, Group '920nm 2PE w/o background' and '1320nm 3PE w/o background' exactly reproduce the pulse energy curves for *the same signal* of 0.1 photons/excitation pulse (Figure 1B). Group '920nm 2PE densely labeled' and '920nm 2PE sparsely labeled' are calculated based on the SBR measured in GCaMP6s-labeled neurons and fluorescein-labeled blood vessels, respectively (Figure 2B). 1320-nm 3PE is assumed to be background-free in the mouse cortex.

**3PM has higher calcium imaging sensitivity and discriminability than 2PM in the deep brain.**

The performance of 1320-nm 3PM calcium imaging was compared to 920-nm 2PM using a time-division multiplexing scheme, which allows the essentially simultaneous recording of calcium dynamics from the same region of interest (ROI) with pixel-wise multiplexed 2PE and 3PE signals (Ouzounov et al., 2017) (Materials and Methods). From the neurons in the shallow mouse cortical layer 2/3 and 4, we obtained nearly identical calcium traces with 2PM and 3PM (Figure 2C upper panel), with a Pearson's correlation factor of 0.98 ± 0.01 (mean ± standard error, calculated from 60 traces, each 75s from neurons located from 200 to 400 μm in depth). The relative ΔF/F of GCaMP6s measured by 1320-nm 3PM is close to that of 920-nm 2PM, with the ratio $(\Delta F/F)_{2P}/(\Delta F/F)_{3P}$ = 1.0±0.25 (mean ± standard deviation, n=904 calcium transients from cells located from 240-450 μm), in close agreement to previous studies (Ouzounov et al., 2019, 2017; Takasaki et al., 2019a).

As the imaging depth increases, however, the 2PM background contributes to the increase of baseline fluorescence of neurons as $F_0' = F_0(1 + 1/\mathrm{SBR})$, which reduces the apparent $\Delta F/F$ to $(1 + 1/SBR)^{-1}$ (assuming time-invariant background). A typical comparison of 3PM and 2PM calcium traces in the deep cortex is shown in Figure 2C lower panel, and the ratios of 2PM to 3PM ΔF/F are shown in Figure 2D. In the transgenic mouse brain (CamKII-tTA/tetO-GCaMP6s) at ~ 4 EALs at 920 nm, the apparent ΔF/F measured by 2PM is approximately half of 3PM, indicating SBR ~ 1, which corroborates with the direct SBR measurement in Figure 2B. The 2P ΔF/F deteriorates rapidly with even larger imaging depth, due to the rapid decline of SBR (e.g., Figure 2B). Similar results have been observed in other densely labeled transgenic lines (Slc17a7/ai162) by independent studies (Takasaki et al., 2019b, 2019a). The cell-to-cell variation of the ratio of 2PM to 3PM ΔF/F is mainly caused by the difference in GCaMP expression level (i.e., dimmer cells have lower SBR than brighter cells at the same depth). Therefore, the decreasing SBR is particularly detrimental for measuring the neuronal activity of the dimmer neurons for deep brain 2PM. Even at 3 EALs (~450 μm), some dimmer neurons already show lower $\Delta F/F$ for 2PM than that for 3PM (Figure 2D).

In addition to the loss of contrast, the noise accompanied by the 2PM background reduces the calcium transient detection accuracy, which is quantified by modifying the expression of d' to include the fluorescence background:

$$d' \approx \frac{\Delta F}{F_0(1 + 1/\mathrm{SBR})}\sqrt{\frac{F_0(1 + 1/\mathrm{SBR})\tau}{2}} = \frac{1}{\sqrt{1 + 1/\mathrm{SBR}}}\frac{\Delta F}{F}\sqrt{\frac{F_0\tau}{2}} \qquad (2)$$

For the same calcium sensitivity ($\Delta F/F$) and baseline cell brightness ($F_0$), the discriminability d' of calcium transients is reduced by a factor of $(1 + 1/\mathrm{SBR})^{1/2}$ in the presence of the background.

For example, when $\mathrm{SBR} = 1$, the d' value is reduced by a factor of 1.4, resulting in a lower true-positive or higher false-positive rate for spike detection. To compensate for the reduced d', $F_0$ needs to be increased by a factor of $(1 + 1/\mathrm{SBR})$, which can only be achieved by increasing the excitation pulse energy by a factor of $(1 + 1/\mathrm{SBR})^{1/2}$ (since 2PE fluorescence $\propto P^2$) or increasing the dwell time on each neuron by a factor of $(1 + 1/\mathrm{SBR})$. Consequently, the cross-over depth between 1320-nm 3PM and 920-nm 2PM for achieving the same d' with the same excitation pulse energy is at a shallower depth (~ 600 μm) than that based only on the signal strength (~ 700 μm), see Figure 1B and Figure 2-figure supplement 2. The SBR of 2PM drops even faster with depth than the exponential decay of the fluorescence signal because, in addition to the decrease of the signal, the background also increases with depth (Figure 2-figure supplement 2) (Theer et al., 2003). Therefore, 2PM imaging significantly beyond the depth where $\mathrm{SBR} = 1$ is impractical.

**Tissue heating and excitation saturation limit the average and peak power.**

Laser-induced tissue damage can be categorized into thermal and nonlinear damage, with distinct mechanisms and dependence on imaging parameters. Continuous heating damages the brain tissue through high temperature, which disturbs various biophysical processes (Podgorski and Ranganathan, 2016). Heating-induced damage happens in the bulk tissue and depends on the average power per illumination volume. On the other hand, nonlinear damage is caused by the strong electric field at the focal point, which is related to focal spot size, pulse energy, and pulse duration.

We used Monte Carlo method to calculate light intensity distribution and temperature rise caused by 1320-nm illumination and compared the simulation to immunohistochemistry results, following

previous works on 2PM brain heating assessment. The previous works showed that brain tissue damage was observed at >250 mW average power of continuous 920-nm illumination in both anesthetized and awake mice with cranial windows (NA=0.8; Linear FOV=1 mm; focal depth=250 µm) (Podgorski and Ranganathan, 2016). In comparison, 1320-nm light experiences stronger water absorption and weaker scattering, which implies higher heat generation in a smaller volume, and therefore tissue temperature is expected to rise faster with input power (Table 2). According to our simulation, at 1 mm imaging depth, the maximum brain temperature starts to rise above the normal body temperature of 37 ℃ at 80 mW average power immediately after the an objective lens of 2-mm work distance (or 68 mW at the brain surface) with continuous scanning (Figure 3B and C; NA~0.75; FOV=230 µm). For power higher than 80 mW, the peak temperature rises at a rate of ~3 ℃ per 50 mW after the objective lens (Figure 3C). At low imaging power, light absorption does not raise the maximum tissue temperature but makes up for part of the heat loss through the cranial window (Podgorski and Ranganathan, 2016). As the input power keeps increasing, the temperature rises almost linearly with input power. The reason to distinguish the average power after the objective lens from that at the brain surface is that the absorption of 1320-nm light by immersion water is not negligible. For objective lenses with different work distances, the average power at the brain surface needs to be re-calibrated according to the actual thickness of immersion water (Figure 3- figure supplement 1-Materials and Methods).

To experimentally determine the tissue heating at various average power, we immunolabeled *post mortem* brain slices of mice after the exposure to 20-minute continuous scanning with 1320-nm 3PM at two imaging depths (1 mm and 1.2 mm, Figure 3D). According to the immunohistochemistry results, no tissue response was detected by measuring heat shock protein

(anti HSP-70/72), microglial (anti-GFAP), or astrocytic activation (anti-Iba1) at 100 mW average power in anesthetized mice (NA=0.75; Linear FOV = 203 µm; n=5 mice, Figure 3- figure supplement 5); however, there is a non-zero chance (1 in 4 mice at 1 mm depth and 1 in 3 mice at 1.2 mm depth) of detectable tissue response with 150 mW imaging power, based on visual inspection of the brain slices (Figure 3D) and the quantification of immunolabeling intensity (Figure 3E). The variation in the levels of activation measured at the same average power in different mice may result from several factors, including the variation in attenuation length and the level of tissue growth 3 weeks after window implantation. Relating to the temperature calculation in Figure 3C, the immunohistochemistry results at 150 mW illumination suggest the upper bound of peak temperature should not exceed 41 ℃, which is the peak temperature at an illumination power of 150 mW, according to our simulation (Figure 3C). Based on this estimated criterion, the maximum allowable imaging power can be interpolated for different imaging depths and FOV, according to Figure 3- figure supplement 3 and Figure 3- figure supplement 4. In general, the maximum brain temperature is lower with larger imaging depth or scanning FOV for the same excitation power.

In addition to 1320 nm, we also simulated brain heating with 1280 nm excitation light since the water absorption coefficient at 1280 nm is ~ 65% of that at 1320 nm (Table 2). As a result, 3PE with 1280 nm allows almost 50% more average power than 1320 nm with similar EAL (Kobat et al., 2009), which is potentially beneficial for maximizing imaging depth or FOV. However, the GCaMP6 sensitivity (ΔF/F) with 1280-nm 3PE *in vivo* is only half of that with 1320 nm, which favors 1320 nm for three-photon calcium imaging (Ouzounov et al., 2019).

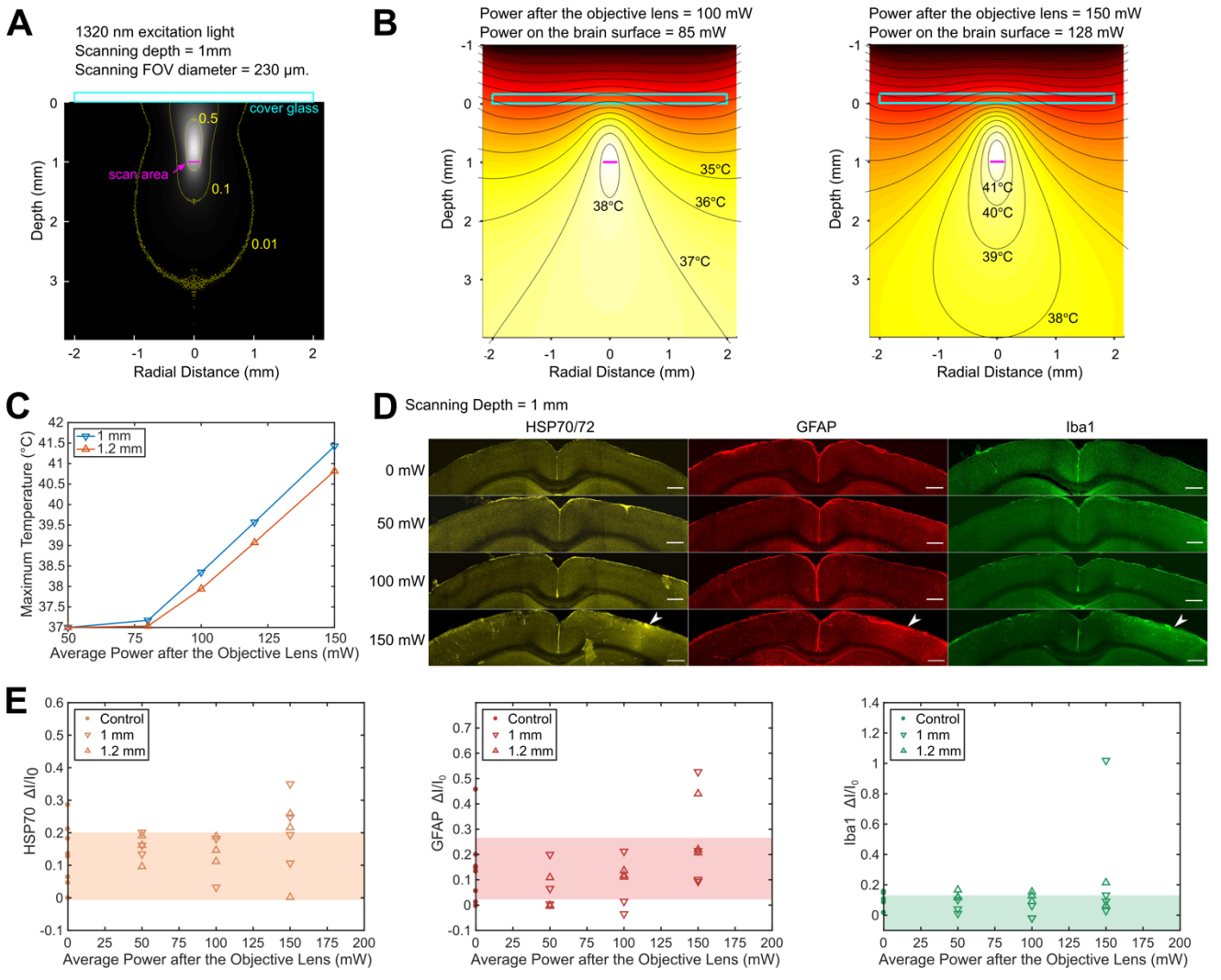


Figure 3. Brain heating and thermal damage induced by continuous scanning by 1320-nm 3PM. (A) Monte Carlo simulation of light intensity of 1320-nm excitation light. The excitation light is focused at 1 mm below the brain surface in the cortex by an objective of 1.05 NA at ~75% filling of its back aperture and scanned telecentrically in a 230-μm diameter FOV (the horizontal magenta line segment). Three iso-contour lines (from inside to outside) correspond to 0.01, 0.1, and 0.5 of the maximum intensity. (B) Temperature maps under 1320-nm illumination calculated from the power absorption per unit volume in (A) after 60 s of continuous scanning with 100 and 150 mW average power after the objective lens. Temperature is color-coded with isotherms plotted at 1 ℃ increment with the highest 4 temperature levels labeled. The average imaging power is listed at the top of each

plot. (C) The maximum temperature versus imaging power for 1 mm and 1.2 mm focal depth, with other imaging parameters the same as in (A) and (B). The maximum temperature is calculated as the average in the hottest volume around the scan area (~$10^7$ µm$^3$). The power at the brain surface can be obtained by multiplying the power after the 2-mm working distance objective lens with 0.85 for 1 mm imaging depth, and 0.89 for 1.2 mm imaging depth. (D) Immunolabeled brain slices of mouse brains after 3PM at 1320 nm with 0, 50 mW, 100 mW, and 150 mW average power (1 mouse is shown for each power). The brain was scanned for 20 minutes continuously at 1 mm below the surface, with 230 µm x 230 µm FOV and 2-Hz frame rate. The location of the damage is indicated by the white arrowheads. Scale bar, 0.5 mm. (E) Quantification of heating-induced damage by the fractional change of immunolabeling intensity relative to the region in the contralateral hemisphere. Shaded areas denote 95% confidence interval of the control group mean (n=4 mice for control; n=6 mice for 50 mW; n=5 mice for 100mW; n=7 mice for 150 mW).

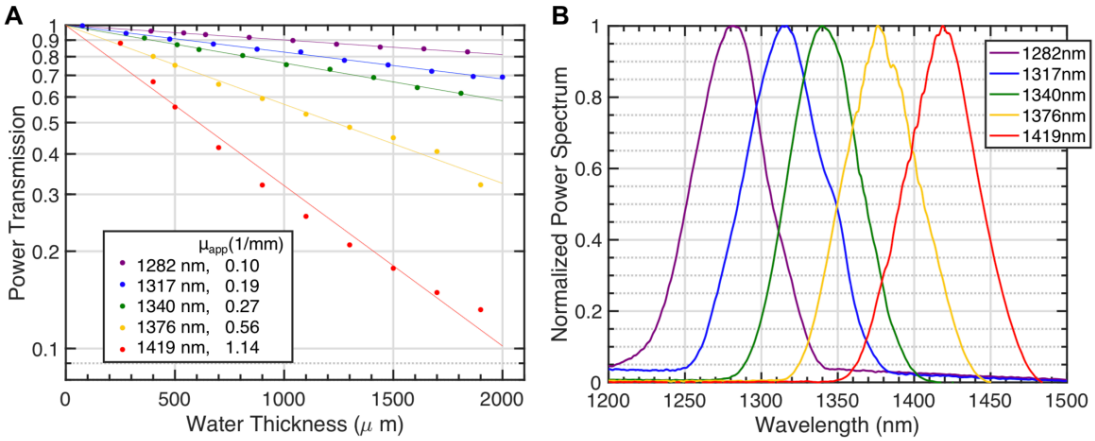


Figure 3- figure supplement 1 Light attenuation by immersion water for various excitation wavelengths.

(A) Power transmission versus immersion water thickness under the objective (Olympus XLPLN25XWMP2, 25X, NA=1.05, ~ 75% filling of the back aperture) for 5 spectra centered from 1280

nm to 1420 nm using broadband pulses from the NOPA. Each transmission curve is fitted with a single exponential function to calculate the apparent attenuation coefficient ($\mu_{app}$). The inset lists these coefficients. (B) The spectra of the pulses for the transmission measurement in (A).

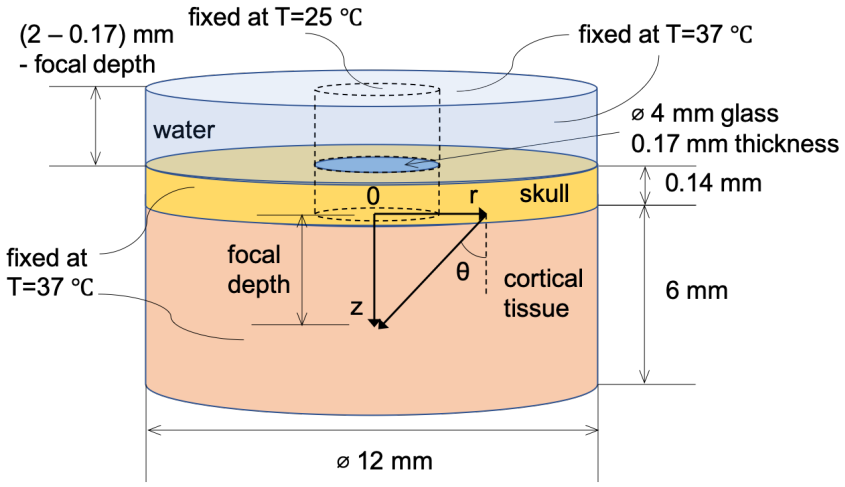


Figure 3- figure supplement 2. Spatial dimension, coordinate system, and boundary conditions for Monte Carlo and heat conduction simulation.

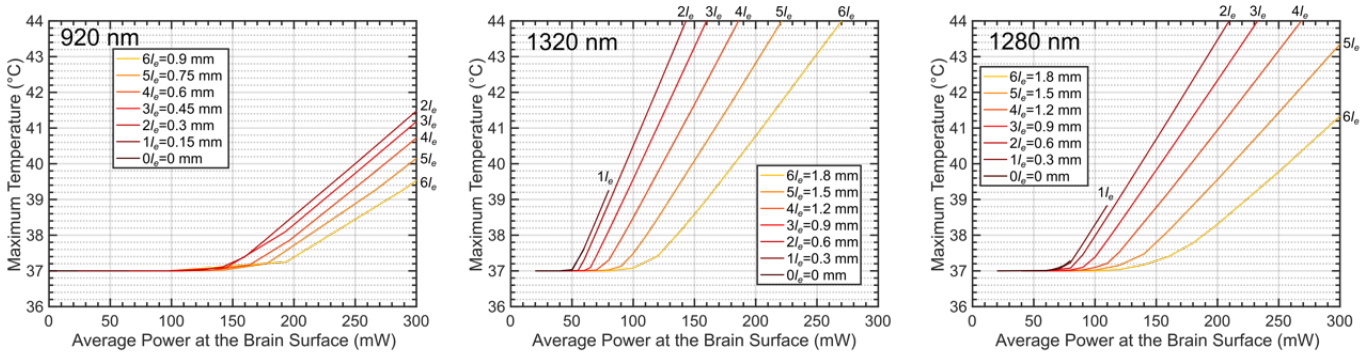


Figure 3- figure supplement 3. The maximum brain temperature as a function of the average power at the brain surface, shown for different imaging depths at 920 nm, 1320 nm, and 1280 nm. The imaging depth grows in the increment of the nominal effective attenuation length of the cortex ($l_e$), which is 150 µm for 920 nm and 300 µm for both 1320 nm and 1280 nm. The linear scanning FOV diameter is 300 µm, and other parameters used for the simulation are listed in Table 2 and Table 3. For 1320 nm, the power immediately after the objective lens can be calculated by multiplying the

power at the brain surface with a factor to correct for immersion water absorption: 1.42, 1.33, 1.27, 1.20, 1.13, 1.07, and 1.01 (from 0 to 6 $l_e$). For 1280 nm, the correction factors are: 1.20, 1.17, 1.13, 1.10, 1.07, 1.03, and 1.00 (from 0 to 6 $l_e$).

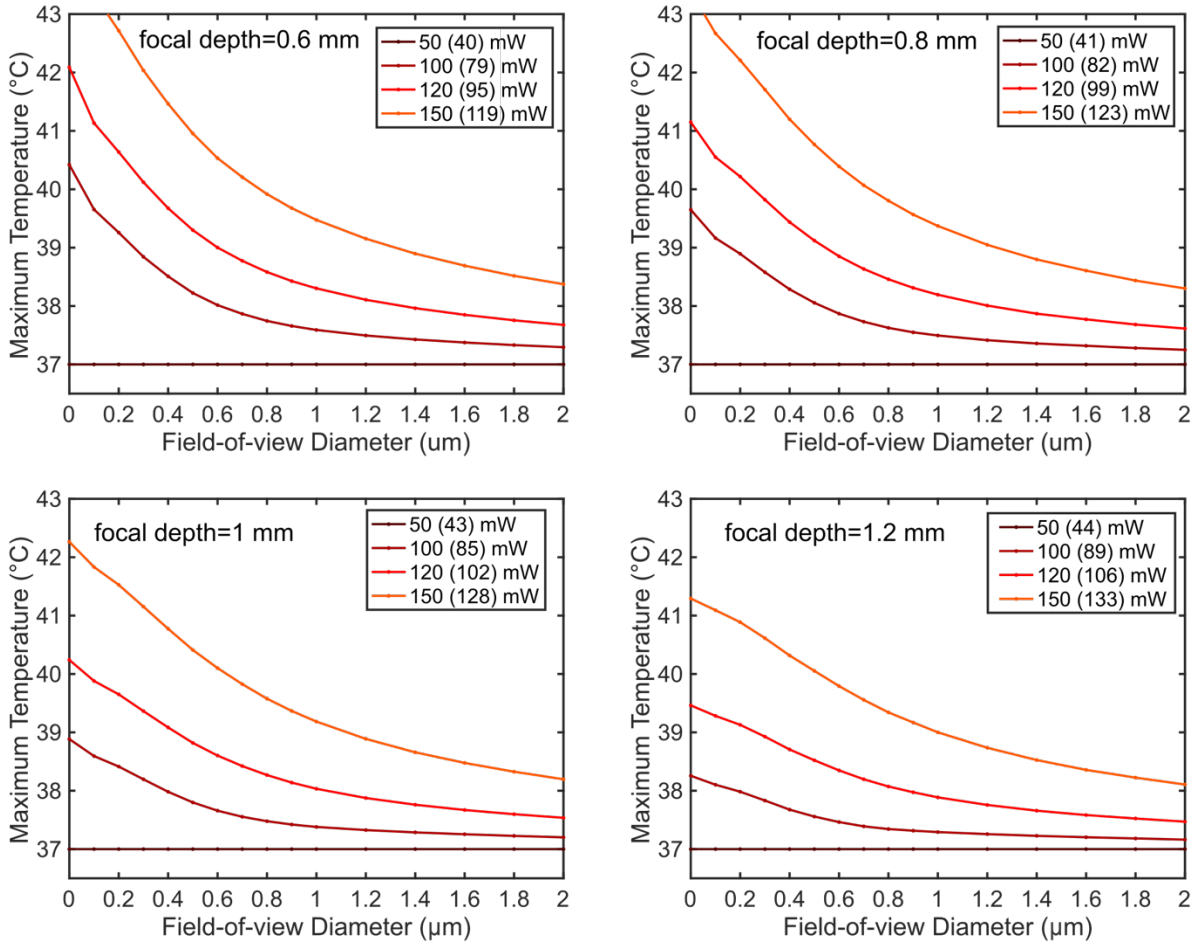


Figure 3- figure supplement 4. The maximum brain temperature decreases with the scanning field-of-view.

The simulation was performed for 1320-nm excitation wavelength at 1- and 1.2-mm imaging depth with various average powers after the objective lens. The NA and the back-aperture beam size remain the same as in Figure 3A. Each legend key indicates the power immediately after the objective lens,

364 followed by the power at the brain surface after immersion water absorption (in the bracket).

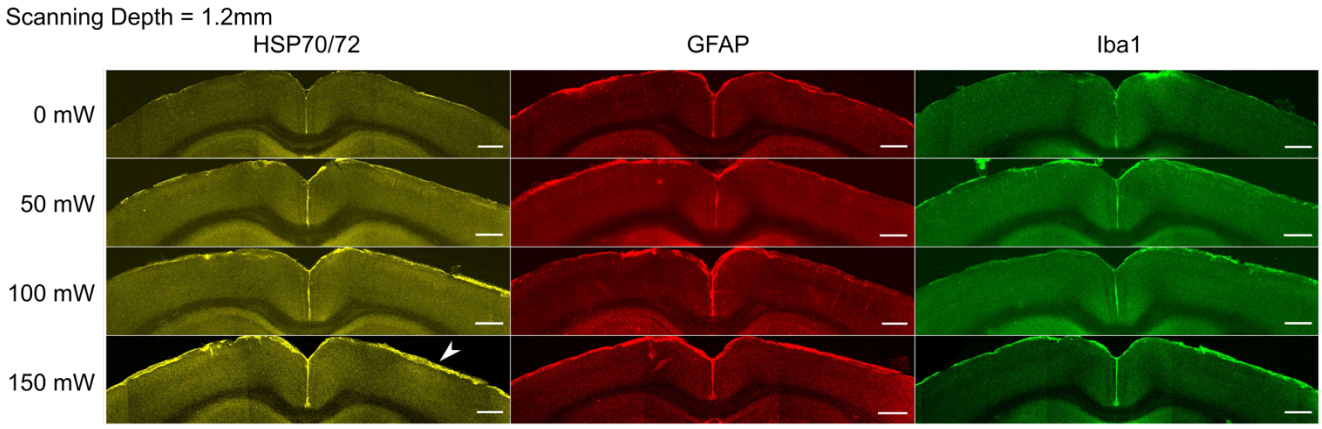


365

366 Figure 3- figure supplement 5. Immunostaining reveals brain tissue damage by 1320-nm 3PM with

367 150 mW imaging power after the objective lens at 1.2-mm imaging depth.

368 The scanning was performed with 230 µm FOV for 20 minutes at various average powers in the

369 mouse brain. The window and scanning area are on the right side of each brain slice, and the location

370 of heating is indicated with white arrowheads. Scale bar, 500 µm.

**Table 1. Percentage of Excitation Photons for Various Final Destinations.**

| | 920 nm | 1320 nm | 1280 nm |
|---|---|---|---|
| Contributing to heating | 20 | 63 | 49 |
| Back scattered to window | 25 | 9 | 10 |
| Back scattered to skull | 20 | 9 | 11 |
| Escaped* | 35 | 19 | 30 |

371 *Photons escape the simulation volume by traveling too far (>6 mm) from the center of the cranial

372 window or too deep (>6 mm) from the tissue surface.

373

374 High peak excitation intensity has several adverse effects on brain imaging, including fluorophore

375 saturation, bleaching, and nonlinear tissue damage. For GCaMP6s, we calculated that

376 fluorescence saturation (i.e., ground-state depletion) occurs at 4-5 nJ under 3PE under our

377 imaging conditions (Materials and Methods). Laser-induced nonlinear damage can be observed in

cells as a sudden but irreversible elevation to extraordinary brightness, which is caused by the rapid ionization and recombination of molecules followed by pressure increase (Tsai et al., 2009). In general, the damage threshold for the peak intensity increases with wavelength (Fu et al., 2006; König et al., 1999; Olivié et al., 2008). Since the area of the focal spot scales as $\lambda^2$, where $\lambda$ is the excitation wavelength, the long wavelength used for 3PM allows higher pulse energy than 2PM. Our previous work showed that neurons remain healthy and viable for weeks after hours of exposure to 1.5 nJ pulses (60 fs and NA~0.75) at the 1300-nm wavelength (Ouzounov et al., 2017). As an estimate of the upper bound of pulse energy, we observed that ~10 nJ at the focus causes tissue ablation, in agreement with another independent study (Yildirim et al., 2019). In addition, it was shown that 1 to 2 nJ pulse energy at the focus (~ 40 fs, NA ~ 1.0) does not appear to alter the physiological response of the neurons under visual stimulation (Yildirim et al., 2019). Based on these results, 1 to 2 nJ pulse energy at the focus is reasonable for 3PM to achieve sufficient signal strength while avoiding nonlinear photodamage and fluorophore saturation.

## Discussion

In this study, we quantitatively compared 1320-nm 3PM and 920-nm 2PM for deep tissue GCaMP6 imaging. The 1320-nm 3PM has the benefit of more efficient signal generation and substantially higher SBR for calcium imaging in the deep mouse brain cortex. We find that 1320 nm 3PM outperforms 2PM in signal generation efficiency at a depth beyond ~ 700 µm in mouse neocortex regardless of the labeling density. In the densely labeled mouse brain, e.g., CaMKII GCaMP6s transgenic mouse, 1320-nm 3PM is preferred beyond the depth where SBR ~ 1 (e.g., ~4 EALs or 600 µm in mice neocortex). In practice, depending on the labeling density and expression

nonuniformity, 3PM might be considered at an even shallower depth to prevent recording bias against neurons with lower expression levels, e.g., ~3 EALs or ~450 µm (Figure 3D).

Based on our results, it is clear that the laser repetition rate should be optimized at different depths to maximize the FOV or the number of neurons recorded. In the shallow region of the brain, the repetition rate should be high for strong signal generation, with the pulse energy kept low to avoid nonlinear damage. For deeper imaging in the brain, where the thermal damage by average power becomes predominant, the repetition rate should be reduced while keeping the average power constant, since the 3PE signal is proportional to $P^3/f^2\tau^2$. For example, when imaging GCaMP6s-labeled at 600 µm depth using 1320 nm 3PE, ~15 nJ pulse energy on the brain surface is required for 0.1 photons/pulse detected (Figure 1B), and the maximum repetition rate to avoid substantial tissue temperature rise is 100mW/ 15nJ = 6.7 MHz, where 100 mW is predicted as a safe power to avoid thermal damage at this imaging depth, given a large enough scanning FOV (Figure 3- figure supplement 3 and Figure 3- figure supplement 4). When imaging the hippocampus at ~ 1 mm depth, the maximum repetition rate has to be reduced to 120 mW/100 nJ = 1.2 MHz, since the pulse energy delivered to the brain surface has to increase exponentially with depth and the white matter has a much smaller attenuation length than the grey matter (Horton et al., 2013; M. Wang et al., 2018).

418 ## Materials and Methods

419 ### Simultaneous 1320-nm 3PM and 920-nm 2PM Imaging with Time Division Multiplex Scheme

420 The excitation source for 1320-nm 3PM was a noncollinear optical parametric amplifier (NOPA,
421 Spectra-Physics) pumped by an ultrafast amplifier (Spirit, Spectra-Physics). The excitation source
422 for 920-nm 2PM was a mode-locked Ti:Sapphire laser (Tsunami, Spectra-Physics). The two
423 excitation beams were launched into a custom-built microscope, described in our previous works
424 (Ouzounov et al., 2019, 2017). The 3PE wavelength was centered at 1320 nm and 2PE at 920 nm
425 for the optimal d' (Ouzounov et al., 2019). The two excitation beams were verified to have similar
426 spatial resolution well below the size of neurons or blood vessels such that their excitation
427 volumes are almost identical (Ouzounov et al., 2019).
428
429 Time-division multiplex (TDM) achieves nearly simultaneous 2PM and 3PM imaging by alternating
430 between spatially overlapped 920-nm and 1320-nm laser beams on a microsecond time scale. 2PE
431 and 3PE fluorescence signals were separated according to the recorded laser clock. More details
432 about the setup can be found in (Ouzounov et al., 2017). The calcium activities were recorded
433 with a 13.6 Hz frame rate. The excitation power for 3PM and 2PM were adjusted to yield similar
434 photon count per frame to yield about the same noise level, and the FOV was reduced to increase
435 the laser dwell time on neuron bodies.
436
437 ### Photon Counting Schemes
438 The microscope was first tested for shot-noise limited performance by photon counting the signal
439 generated by stationary 1320-nm or 920-nm beam focused in fluorescein solution (~40 µM and
440 pH=10). The laser power was chosen (~0.3 mW for both wavelengths) to ensure the photon

counts per second is lower than 5% of the laser repetition rate of the NOPA, which limits the photon stacking error to within 2.5% of the total counts. According to Poisson statistics, photon stacking error causes a fraction of $1-(1-e^{-\lambda})/\lambda$ underestimation in photon counts, where λ is the average count per second divided by the laser repetition rate. For Ti:Sapphire, the photon stacking error is negligible since the typical photon counts are below 1% of its repetition rate (80MHz). In this experiment, the PMT (Hamamatsu H7422-40) anode current was first amplified with a 10MHz bandwidth pre-amplifier (C9999, Hamamatsu), and then counted by a photon counter (SR400, Stanford Research). Shot-noise limited performance was confirmed for our imaging system.

During imaging, the photon counts of neurons were obtained by converting pixel values to photon counts according to a conversion factor. The calibration was done by parking a 920-nm or 1320-nm focus in a fluorescein sample and then perform photon counting and imaging consecutively. Linearity between pixel values and photon counts were tested by changing the laser power, and the ratio between them was used as the conversion factor. In fact, recording analog value is a better way to measure high photon counts, since there is no photon stacking error and the voltage signal can simply be summed. The conversion factor was further confirmed by observing the first mode in a pixel value histogram. The zeroth mode of a pixel histogram peaks at PMT offset value, and the first mode is larger than that, representing pixels receiving exactly one photon. Higher-order modes can also be observed, representing pixels receiving multiple photons. For all simultaneous 2P and 3P imaging, the sampling frequency was 5 MHz, so that direct photon counting based on images could also be performed, which showed consistent results in comparison to analog recordings.

464 **Measurement of Excitation light Attenuation in the Brain Tissue Based on Fluorescence Signal**

465 The vasculature imaging was performed simultaneously with 2PM and 3PM using the TDM
466 scheme. The image stack was taken with 10 μm step size in depth, and the imaging power was
467 increased with imaging depth to keep the signal level approximately constant. The signal of each
468 frame was calculated as the average of the brightest 0.5% pixel values and then converted to
469 photon counts per excitation pulse according to the method described in the previous section.
470 The fraction of excitation power reaching the focus from the brain surface (Focus Power/Surface
471 Power) was calculated as the square (cubic) root of the ratio of the 2PE (3PE) signal at the imaging
472 depth and at the brain surface.

473

474 **Measurement of the Pulse Energy Required per 0.1 Photon Detection**

475 To have a fair comparison on the excitation efficiency of 920-nm 2PM and 1320-nm 3PM, we
476 controlled all the parameters regarding 2PE and except for the wavelength. For both wavelengths,
477 the axial resolution was made equal by adjusting the beam size at the back aperture of the
478 objective separately. The point spread functions of both wavelengths were also overlapped
479 laterally (by fine-tuning the 920-nm beam pointing direction) and axially (by changing the field
480 curvature of the 920-nm beam at the objective lens back aperture by slight adjustment of the
481 distance between the lenses of a 1:1 telescope). For both wavelengths, the pulse durations were
482 scaled to 60 fs (measured pulse durations were 60-70 fs in FWHM for 1320-nm, and 180-200 fs for
483 920-nm. All pulses were assumed to have $\text{sech}^2$ profile). Light absorption by the immersion water
484 was taken into account when calculating the pulse energy for 1320 nm on the brain surface. As we
485 show in Figure 3- figure supplement 1, it is important to distinguish the pulse energy on the brain
486 surface and after the objective lens for 1320 nm excitation.

Based on the fluorescence signals derived from simultaneous 2P and 3P imaging, Figure 1B was plotted using the following equations (Xu and Webb, 1997):

$$S_{2P}/f = C_2(P/f)^2/\tau \quad (3)$$

$$S_{3P}/f = C_3(P/f)^3/\tau^2 \quad (4)$$

where $S_{nP}/f$ is the n-photon-excited signal yield in the unit of detected photons/pulse, $P$ is the average power at the brain surface, $f$ is the repetition rate, τ is the pulse duration, and $C_n$ (n=2 and 3) are the coefficients to be determined. For vasculature imaging, $S_{nP}/f$ is calculated as the average of the brightest 0.5% pixel values per frame, converted to photon counts. For GCaMP6s-labeled neurons, $S_{nP}/f$ was calculated from the sum of time-averaged pixel values in cell bodies (averaging time = 75 s, on 37 different cells in 5 animals). Given that $P/f$ and $\tau$ are already measured during the experiment, $C_n$ can be solved. To produce Figure 1B, we plugged $C_n$ into the equations and set the signal yield (i.e., $S_{nP}/f$ ) to 0.1 photons per pulse, pulse duration to 60 fs, and then solve for pulse energy $P/f$ on the sample surface according to Equations 2 and 3.

To account for the EAL variation recorded from different animals inFigure 1B, we measured the effective attenuation length (EAL) of the cortical layers of each animal by imaging fluorescein-labeled blood vessels immediately after calcium imaging. The depths of neurons were rescaled by dividing the measured EAL and then multiplying with the nominal EAL (i.e., 293 μm for 1320 nm 3PE and 154 μm for 920 nm, as measured by the vasculature data). The logarithm of the neuron signal was plotted against depth, and then fitted with a linear model for the slope and intercept (Figure 1B). The slope equals $ln(10)/\mathrm{EAL}$, and the intercept equals to the pulse energy required to yield 0.1 detected photon per pulse on the sample surface (i.e., zero imaging depth).

### Measurement of Signal-to-background Ratio

The signal of each frame was measured as the average of the brightest 0.1% pixel values. For vasculature data, the background was measured as the average pixel values of regions surrounding the blood vessels (i.e., not labeled). For GCaMP6 neural data, the background was measured as the pixel value in the shadow of big blood vessels. The pixel values of cortical tissue surrounding the neurons cannot be used as background since it contains densely labeled neuronal processes except for area within the blood vessels. SBR was calculated as the signal divided by the background.

### Quantification of Vasculature Volume Fraction and Staining Inhomogeneity

The SBR limit of 2PM depends on the spatial inhomogeneity of staining (Theer and Denk, 2006). We quantified the staining inhomogeneity of fluorescein-labeled vasculature in order to compare the *in vivo* SBR measurement to the theory and *ex vivo* fluorescent beads measurement (Theer and Denk, 2006). The volume fraction of the vasculature can be estimated by the fraction of the stained blood vessel area in each xy image frame. Figure 2-figure supplement 1 shows the fractional vascular area vs. imaging depth, derived from the same 3PM dataset, as in Figure 2B. The segmentation of blood vessel regions was performed with *graythresh* function in MATLAB and then inspected manually for correctness. We concluded that the labeled vascular volume accounts for 2 ± 1% (mean ± standard deviation) in the imaged column of the mouse cortex (~2mm lateral and 2mm caudal to the Bregma point, Figure 2B). Our result is in close agreement with other studies quantifying the fractional vascular volume by imaging sliced brains *ex vivo* (~2% for blood vessels of 20 µm or less diameter in the primary somatosensory cortex) (Wang et al., 2019; Xiong et al., 2017). We noticed that most of the blood vessels in the imaged volume has a diameter of less than 20 µm, except for a few on the brain surface (Figure 2-figure supplement 1A). The blood

vessel density is lower in the white matter (~750-850 μm) than that in the cortex (Figure 2-figure supplement 1B). The staining inhomogeneity is defined as , $\chi = \hat{C}/\langle C \rangle$, where $C = C(x, y, z)$ denotes the spatial distribution of dye concentration in the entire imaged volume, $\hat{C}$ is the maximum concentration, and $\langle C \rangle$ is the average concentration (Theer and Denk, 2006). Staining inhomogeneity can be estimated as 1/(factional vascular volume) with the assumption that all the labeled blood vessels are equally bright (C=1 for all vasculature), and the rest of tissue is completely unstained (C=0 for the rest). Our experiments show that 2PM reaches SBR of 1 at about 4.7 $l_e$, i.e., 730 μm with $l_e$ =154 μm (Figure 2B). This result is in close agreement to the 4.7 $l_e$ predicted by theoretical calculation with a staining inhomogeneity of 50 (Theer and Denk, 2006).

## Analysis of the Calcium Traces of Neurons

Sample motion in the original images, if any, was corrected by TurboReg plug-in in ImageJ. Regions of interest (ROIs) were generated by manual segmentation of neuron bodies. The pixel values of ROIs were exported to MATLAB 2016b for further processing. All the pixels in the ROI were summed and converted to photon counts. Spikes were inferred by thresholding the Poisson-distribution-based likelihood function derived from each trace (Wilt et al., 2013). The discrimination threshold was chosen to be C=ln((1-r)/r), where r is the estimated firing rate, which was estimated for each individual trace as the fraction of the trace that is more than 1.5 standard deviation above its mean. The baseline ($F_0$) was determined by averaging trace values, after excluding the spikes and their rising and falling edges. For the processed traces in Figure 1C, fluorescence intensity traces were low-pass filtered with a hamming window of a time constant of 0.37 s. Traces (F) were normalized according to the equation $(F- F_0)/F_0$.

554 **Measurement of ΔF/F ratio from Simultaneously Recorded 3PM and 2PM Calcium Traces**

555 Based on the low-pass-filtered and normalized calcium traces described in the section above, the
556 peaks of spikes were detected by finding local maxima that are larger than 30% ΔF/F in 3PM traces
557 and have corresponding spike peaks detectable in 2PM traces. To produce the plot of Figure 2D,
558 the ratios of 2PM and 3PM ΔF/F, i.e., $(\Delta F/F)_{2P}/(\Delta F/F)_{3P}$, of the same calcium transients were taken,
559 and the depth of each neuron was normalized with the EAL of each animal.

560

561 **Monte Carlo Simulation of Light Propagation and Validation of Tissue Optical Parameters**

562 We used Monte Carlo simulation to calculate light propagation in the brain tissue, following the
563 algorithm described previously (Stujenske et al., 2015). Podgorski *et al.* adapted the same
564 numerical recipe to predict tissue temperature change during two-photon imaging, which agreed
565 well with experimental measurements at the wavelengths of 800 nm, 920 nm, and 1064 nm
566 (Podgorski and Ranganathan, 2016). In order to simulate for 1320 nm and 1280 nm excitation, we
567 measured and estimated brain optical parameters as follows: For excitation wavelength longer
568 than 1200 nm, water accounts for the majority of the light absorption in brain tissue *in vivo*
569 (Jacques, 2013). Therefore, tissue absorption coefficients $\mu_a$ was approximated with 75% of the
570 spectrum-weighted water absorption coefficient (defined in Section Measurement of Optical
571 Absorption by Immersion Water), and the 75% is based on the water content of brain tissue
572 (Jacques, 2013; Tschöp et al., 2013). Tissue scattering coefficients $\mu_s$ were then calculated from
573 our measured effective attenuation lengths according to $l_e = 1/(\mu_a+\mu_s)$, with $l_e$ =150 μm at 920 nm,
574 and 300 μm at 1320 nm and 1280 nm. As cross-validation, the calculated scattering coefficient at
575 1320 nm is close to that measured by Gebhart *et al.* (i.e., 3.0 $mm^{-1}$) (Gebhart et al., 2006). We
576 assumed an anisotropy factor g = 0.9 and tissue refractive index n = 1.36 for 920 nm, 1280 nm,

577 and 1320 nm, since their variation in the wavelength range of interest is negligible. All the tissue
578 optical parameters are summarized in Table 2.

**Table 2. Optical Parameters of Grey Matter.**

| Variable | Parameter | Wavelength | Value | Units |
|---|---|---|---|---|
| $\mu_a$ | absorption coefficient | 920 | 0.039 | 1/mm |
| | | 1280 | 0.078 | 1/mm |
| | | 1320 | 0.12 | 1/mm |
| $\mu_s$ | scattering coefficient | 920 | 6.7 | 1/mm |
| | | 1280 | 3.2 | 1/mm |
| | | 1320 | 3.2 | 1/mm |
| $g$ | anisotropy coefficient | All | 0.9 | dimensionless |
| $n$ | refractive index | All | 1.36 | dimensionless |

579

580 To simulate underfilling of the objective back aperture, we initialized random photon distribution
581 incident to the brain surface according to the relations:

$$w = w_0\sqrt{-1/2\ln(X)}$$
$$\theta = \sin^{-1}(w/n_0 f) \quad (5)$$
$$r = \tan(\theta)\, z$$

582

583 where $X$ is a random variable drawn from a uniform distribution from 0 to 1, $w_0$ is the $1/e^2$ beam
584 radius of the Gaussian beam at the objective back aperture, $w$ is the radial distance to the
585 objective optical axis of a randomly generated photon conforming to the Gaussian beam profile
586 mentioned above, $f$ is the objective focal length, $n_0$ is the refractive index of immersion water, z is
587 the imaging depth in the sample. r and θ define, respectively, the radial coordinate of photon
588 position and the polar angle of propagation direction, both with respect to the objective optical
589 axis (Figure 3- figure supplement 2). The objective (Olympus XLPLN25XWMP2, 25X, NA=1.05, f=7.2
590 mm) is under-filled, with 70% of its back aperture matched to the $1/e^2$ beam diameter of a

591 Gaussian beam, which gives an effective NA of ~ 0.75 (Theer and Denk, 2006). The geometry of
592 the simulation volume and boundary conditions are shown in Figure 3- figure supplement 2.
593
594 **Heat Diffusion Model with Bio-heat Equation**
595 Using the light intensity as the heat source, we calculated the temperature distribution by solving
596 numerically the bio-heat equation (6), identical to that used previously by Stujenske *et al.*
597 (Stujenske et al., 2015):

$$\rho c \frac{\partial T(\vec{r},t)}{\partial t} = k\nabla^2 T(\vec{r},t) + \rho_b c_b w_b \left(T_A - T(\vec{r},t)\right) + S_h(\vec{r}) + q_m \quad (6)$$

598 where $T(\vec{r},t)$ is the spatial-temporal temperature distribution, $S_h(\vec{r})$is the radiative heat
599 generation from Monto Carlo simulation, and the rest of the parameters and their values are
600 listed in Table 3, which are the same as in ref. (Stujenske et al., 2015).

**Table 3. Thermal and Mechanical Properties of Grey Matter (Stujenske et al., 2015).**

| Variable | Parameter | Value | Units |
|---|---|---|---|
| $\rho$ | density | $1.04\times10^{-3}$ | g/mm$^3$ |
| $c$ | Brain specific heat | $3.65\times10^{3}$ | mJ/g°C |
| $k$ | Thermal conductivity | 0.527 | mW/mm °C |
| $\rho_b$ | Blood density | $1.06\times10^{-3}$ | g/mm$^3$ |
| $c_b$ | Blood specific heat | $3.6\times10^{3}$ | mJ/g°C |
| $w_b$ | Blood perfusion rate | $8.5\times10^{-3}$ | /s |
| $q$ | Metabolic heat | $9.5\times10^{-3}$ | mW/mm$^3$ |
| $T_A$ | Arterial temperature | 36.7 | °C |

601
602 We calculated steady-state temperature distribution at various imaging depths (0-6 attenuation
603 lengths) and average powers for 920 nm, 1320 nm, and 1280 nm. Figure 3- figure supplement 3
604 shows the maximum tissue temperature as a function of the average input power on the brain

surface. The maximum temperature is evaluated as the average temperature in a volume of ~$10^7$ $\mu m^3$ (Figure 3- figure supplement 3), or equivalent to a cylinder of ~120-µm radius and ~210-µm height enclosing the hottest region of the tissue. The power at the brain surface is calculated from the power immediately after the objective lens by taking account of the absorption by immersion water.

## Immunohistology for Assessing Thermal Damage Induced by 1320nm Illumination

The experiment was performed 3 weeks after the window implantation. Anesthetized (2% isoflurane mixed with oxygen) mice were exposed to continuous scanning for 20 min at a 2-Hz frame rate and 230 µm x 230 µm FOV, similar to 3PM of neural activity at 1320-nm. After 18 hours, mice were perfused with 4% paraformaldehyde, and post fixed in the same solution for 24 hours, followed by sucrose solutions immersion (10%, 20%, and 30% incrementally). Scanned brain regions were coronally sectioned into 200 µm sections and blocked at room temperature. Alternating slices were incubated at 4 ℃ overnight, with primary antibodies for heat shock protein (HSP70/72), glial fibrillary acidic protein (GFAP), and Iba1. Primary antibodies used were mouse monoclonal anti-HSP70/72 (C92F3A-5) (ADI-SPA-810-F, Enzo, 1: 400 dilution), mouse anti-GFAP (G3893, Sigma-Aldrich, 1:760 dilution), and mouse anti-Iba1 (SAB2702364, Sigma-Aldrich, 1: 1000). Slices were washed and incubated with secondary antibody conjugated to Alexa Fluor 546 (A11003, ThermoFisher,1:500 dilution) at 4 ℃ overnight , washed again, and mounted in VECTASHIELD antifade medium for confocal imaging. Images were analyzed with ImageJ. The intensity ($I_0$) was determined by the average intensity in the region of interest ~1 mm wide centered around the illuminated site covering the entire thickness of the neocortex, and the baseline ($I_0$) was determined in the mirror position in the contralateral hemisphere. The level of

tissue response was quantified as the fractional change of immunolabeling intensity relative to the region of contralateral hemisphere: $(I- I_0)/I_0$. The procedures described here follows closely the previous studies on assessing thermal damage caused by 2-photon imaging of mouse brain (Podgorski and Ranganathan, 2016).

## Calculation of the Pulse Energy for Fluorophore Saturation under Three-photon Excitation

At high excitation intensity, the excitation probability per pulse per fluorophore can be so high that some fluorophores will not decay to the ground state before the arrival of the next excitation pulse (Xu and Webb, 1997). The excitation probability per pulse for a fluorescent molecule at the center of the focus is calculated as (Xu and Webb, 1997):

$$\mathrm{Pr} = 1 - \exp\left[-\frac{g_p^{(3)}}{\tau^2}\sigma_3\left(\frac{\mathrm{NA}^2\pi}{\lambda_{3\mathrm{P}}^2}\right)^3\left(\frac{P_{3\mathrm{P}}}{f}\right)^3\right] \quad (7)$$

Where the definition and values of all the parameters remain the same as in the previous section. Using GCaMP6s 3PE cross section of $3\times10^{-82}$ $cm^6s^2$, the pulse energy (i.e., $\frac{\boldsymbol{P}_{3\mathrm{P}}}{\boldsymbol{f}}\cdot\frac{\boldsymbol{hc}}{\boldsymbol{\lambda}_{\mathbf{3P}}}$) required for 10% and 63% excitation probability per pulse is 2 nJ and 4.3 nJ, respectively. We note that these pulse energies are much smaller (by ~ 2π) than those given by Yildirim *et al.* (Yildirim et al., 2019). This factor of 2π error in ref. (Yildirim et al., 2019) is probably due to a typo (the Planck's constant $\boldsymbol{h}$ and $\hbar$**)** since the correct equation for 2PE saturation intensity was given by the same authors in earlier work (So et al., 2000).

## Animal Procedures

Chronic craniotomy was performed on mice according to the procedures described in (Ouzounov et al., 2017). Windows of 5-mm diameter were centered at ~2.5 mm lateral and ~2 mm caudal

from the bregma point over the somatosensory cortex. Vasculature imaging was performed on wild-type mice (8-15 weeks, male, C57BL/6J, The Jackson Laboratory) with retro-orbital injection of fluorescein dextran conjugate (10 kDa, 25 mg dissolved in 200 µl saline). Calcium imaging was performed on five different transgenic animals with GCaMP6s-labeled neurons (3 males and 2 females, 11-17 weeks, CamKII-tTA/tetO-GCaMP6s). The spontaneous calcium activity imaging was performed on awake or lightly anesthetized (0.5-1% isoflurane mixed with oxygen) animals. Thermal damage experiments were performed on wild-type mice (3 to 4 mice for each depth and power combination, for a total of 23 mice, 8-30 weeks, male, C57BL/6J, The Jackson Laboratory). All animal experimentation and housing procedures were conducted in accordance with Cornell University Institutional Animal Care and Use Committee guidance.

## Acknowledgments

We thank Dr. Kaspar Podgorski for sharing the code for brain heating simulation and the protocol for immunohistochemistry. We also thank Dr. Peter So for the discussion on three-photon excitation saturation. This work has been supported by National Science Foundation (DBI-1707312, Neuronex Hub), Intelligence Advanced Research Projects Activity (D16PC00003), National Institutes of Health (DP2MH109982), and Cornell Neurotech Mong Fellowships.

## Competing interests

The authors declare no conflict of interests.

## References


Attardo A, Fitzgerald JE, Schnitzer MJ. 2015. Impermanence of dendritic spines in live adult CA1 hippocampus. *Nature* **523**:592–596. doi:10.1038/nature14467

Chen Bi, Huang X, Gou D, Zeng J, Chen G, Pang M, Hu Y, Zhao Z, Zhang Y, Zhou Z, Wu H, Cheng H, Zhang Z, Xu C, Li Y, Chen L, Wang A. 2018. Rapid volumetric imaging with Bessel-Beam three-photon microscopy. *Biomed Opt Express* **9**:3427–3433.

Chen T-W, Wardill TJ, Sun Y, Pulver SR, Renninger SL, Baohan A, Schreiter ER, Kerr R a, Orger MB, Jayaraman V, Looger LL, Svoboda K, Kim DS. 2013. Ultrasensitive fluorescent proteins for imaging neuronal activity. *Nature* **499**:295–300. doi:10.1038/nature12354

Cheng L-C, Horton NG, Wang K, Chen S-J, Xu C. 2014. Measurements of multiphoton action cross sections for multiphoton microscopy. *Biomed Opt Express* **5**:3427–33. doi:10.1364/BOE.5.003427

Dana H, Mohar B, Sun Y, Narayan S, Gordus A, Hasseman JP, Tsegaye G, Holt GT, Hu A, Walpita D, Patel R, Macklin JJ, Bargmann CI, Ahrens MB, Schreiter ER, Jayaraman V, Looger LL, Svoboda K, Kim DS. 2016. Sensitive red protein calcium indicators for imaging neural activity. *Elife* **5**:1–24. doi:10.7554/eLife.12727

Dana H, Sun Y, Mohar B, Hulse BK, Kerlin AM, Hasseman JP, Tsegaye G, Tsang A, Wong A, Patel R, Macklin JJ, Chen Y, Konnerth A, Jayaraman V, Looger LL, Schreiter ER, Svoboda K, Kim DS. 2019. High-performance calcium sensors for imaging activity in neuronal populations and microcompartments. *Nat Methods* **16**:649–657. doi:10.1038/s41592-019-0435-6

Dombeck D a, Harvey CD, Tian L, Looger LL, Tank DW. 2010. Functional imaging of hippocampal place cells at cellular resolution during virtual navigation. *Nat Neurosci* **13**:1433–40. doi:10.1038/nn.2648

Escobet-Montalbán A, Gasparoli M. F, Nylk J, Liu P, Yang Z, Dholakia K. 2018. Three-photon light-sheet fluorescence microscopy. *Opt Lett* **43**:5484–5487.

Fu Y, Wang H, Shi R, Cheng J. 2006. Characterization of photodamage in coherent anti-Stokes Raman scattering microscopy. *Opt Express* **14**:3942–3951.

Gebhart SC, Lin WC, Mahadevan-Jansen A. 2006. In vitro determination of normal and neoplastic human brain tissue optical properties using inverse adding-doubling. *Phys Med Biol* **51**:2011–2027. doi:10.1088/0031-9155/51/8/004

Horton N, Wang K, Kobat D, Wise FW, Xu C. 2013. In Vivo Deep Penetration Three-Photon Imaging of Mouse Brain through an Unthinned, Intact SkullOptics in the Life Sciences. Optical Society of America. p. NT3B.3. doi:10.1364/NTM.2013.NT3B.3

Inoue M, Takeuchi A, Manita S, Horigane S, Sakamoto M, Kawakami R, Yamaguchi K, Otomo K, Yokoyama H, Kim R, Yokoyama T, Takemoto-Kimura S, Abe M, Okamura M, Kondo Y, Quirin S, Ramakrishnan C, Imamura T, Sakimura K, Nemoto T, Kano M, Fujii H, Deisseroth K, Kitamura K, Bito H. 2019. Rational Engineering of XCaMPs, a Multicolor GECI Suite for In Vivo Imaging of Complex Brain Circuit Dynamics. *Cell* **177**:1–15. doi:10.1016/j.cell.2019.04.007

Jacques SL. 2013. Optical Properties of Biological Tissues: A Review. *Phys Med Biol* **58**:R37-61. doi:10.1088/0031-9155/58/11/R37

Kobat D, Durst ME, Nishimura N, Wong AW, Schaffer CB, Xu C. 2009. Deep tissue multiphoton microscopy using longer wavelength excitation. *Opt Express* **17**:13354–64.

Kobat D, Horton NG, Xu C. 2011. In vivo two-photon microscopy to 1.6-mm depth in mouse cortex. *J Biomed Opt* **16**:106014. doi:10.1117/1.3646209

Kondo M, Kobayashi K, Ohkura M, Nakai J, Matsuzaki M. 2017. Two-Photon calcium imaging of the medial prefrontal cortex and hippocampus without cortical invasion. *Elife* **6**:1–20.

doi:10.7554/eLife.26839
König K, Becker TW, Fischer P, Riemann I, Halbhuber K-J. 1999. Pulse-length dependence of cellular response to intense near-infrared laser pulses in multiphoton microscopes. *Opt Lett* **24**:113. doi:10.1364/OL.24.000113
Lin MZ, Schnitzer MJ. 2016. Genetically encoded indicators of neuronal activity. *Nat Neurosci* **19**:1142–1153. doi:10.1038/nn.4359
Liu H, Deng X, Tong S, He C, Cheng H, Zhuang Z, Gan M, Li J, Xie W, Qiu P, Wang K. 2019. In Vivo Deep-Brain Structural and Hemodynamic Multiphoton Microscopy Enabled by Quantum Dots. *Nano Lett* **19**:5260–5265. doi:10.1021/acs.nanolett.9b01708
Low RJ, Gu Y, Tank DW. 2014. Cellular resolution optical access to brain regions in fissures: Imaging medial prefrontal cortex and grid cells in entorhinal cortex. *Proc Natl Acad Sci* **111**:18739–18744. doi:10.1073/pnas.1421753111
Macklin J, Harris T. 2016a. Linear optical properties and two-photon action cross sections for GCaMP6f and RCaMP1he.
Macklin J, Harris T. 2016b. Three-photon action spectra of GCaMP6f, and the absorption coefficient of water.
Odríguez CRR. 2018. Three-photon fluorescence microscopy with an axially elongated Bessel focus. *Opt Lett* **43**:1914–1917.
Olivié G, Giguère D, Vidal F, Ozaki T, Kieffer J-C, Nada O, Brunette I. 2008. Wavelength dependence of femtosecond laser ablation threshold of corneal stroma. *Opt Express* **16**:4121. doi:10.1364/OE.16.004121
Ouzounov DG, Wang T, Wang M, Feng DD, Horton NG, Cruz-Hernández JC, Cheng Y-T, Reimer J, Tolias AS, Nishimura N, Xu C. 2017. In vivo three-photon imaging of activity of GCaMP6-labeled neurons deep in intact mouse brain. *Nat Methods* **14**:388–390. doi:10.1038/nmeth.4183
Ouzounov DG, Wang T, Wu C, Xu C. 2019. GCaMP6 ΔF/F dependence on the excitation wavelength in 3-photon and 2-photon microscopy of mouse brain activity. *Biomed Opt Express* **10**:3343. doi:10.1364/BOE.10.003343
Perillo EP, Jarrett JW, Liu Y, Hassan A, Fernée DC, Goldak JR, Bonteanu A, Spence DJ, Yeh H, Dunn AK. 2017. Two-color multiphoton in vivo imaging with a femtosecond diamond Raman laser. *Nat Publ Gr* 1–8. doi:10.1038/lsa.2017.95
Pilz G-A, Carta S, Stauble A, Ayaz A, Jessberger S, Helmchen F. 2016. Functional Imaging of Dentate Granule Cells in the Adult Mouse Hippocampus. *J Neurosci* **36**:7407–7414. doi:10.1523/JNEUROSCI.3065-15.2016
Podgorski K, Ranganathan G. 2016. Brain heating induced by near-infrared lasers during multiphoton microscopy. *J Neurophysiol* **116**:1012 LP – 1023.
Rowlands CJ, Park D, Bruns OT, Piatkevich KD, Fukumura D, Jain RK, Bawendi MG, Boyden ES, So PTC. 2017. Wide-field three-photon excitation in biological samples. *Light Sci Appl* **6**:e16255-9. doi:10.1038/lsa.2016.255
So PTC, Dong CY, Masters BR, Berland KM. 2000. Two-photon excitation microscopy. *Annu Rev Biomed Eng* **2**:399–429. doi:10.1016/S1076-5670(03)80016-2
Sofroniew NJ, Flickinger D, King J, Svoboda K. 2016. A large field of view two-photon mesoscope with subcellular resolution for in vivo imaging. *Elife* **5**:1–20. doi:10.7554/eLife.14472
Stirman JN, Smith IT, Kudenov MW, Smith SL. 2016. Wide field-of-view, multi-region, two-photon imaging of neuronal activity in the mammalian brain. *Nat Biotechnol* **34**:857–862. doi:10.1038/nbt.3594
Stujenske JM, Spellman T, Gordon JA. 2015. Modeling the Spatiotemporal Dynamics of Light and Heat

760 Propagation for In Vivo Optogenetics. *Cell Rep* **12**:525–534. doi:10.1016/j.celrep.2015.06.036
761 Takasaki K, Abbasi-Abl R, Waters J. 2019a. Superficial bound of the depth limit of 2-photon imaging in
762 mouse brain. *bioRxiv* 618454. doi:10.1101/618454
763 Takasaki K, Larkin J, Abbasi-asl R, Denman D, Millman D, Vries S De, Takeno M, Costa NM, Reid RC,
764 Waters J. 2019b. 3-Photon Calcium Imaging of Deep Cortical Layers for Functional
765 ConnectomicsBiophotonics Congress: Optics in the Life Sciences Congress
766 (BODA,BRAIN,NTM,OMA,OMP). p. BM4A.4.
767 Theer P, Denk W. 2006. On the fundamental imaging-depth limit in two-photon microscopy. *J Opt Soc*
768 *Am A* **23**:3139–3149.
769 Theer P, Hasan MT, Denk W. 2003. Two-photon imaging to a depth of 1000 microm in living brains by
770 use of a Ti:Al2O3 regenerative amplifier. *Opt Lett* **28**:1022–4.
771 Tischbirek C, Birkner A, Jia H, Sakmann B, Konnerth A. 2015. Deep two-photon brain imaging with a
772 red-shifted fluorometric Ca $^{2+}$ indicator. *Proc Natl Acad Sci* **112**:11377–11382.
773 doi:10.1073/pnas.1514209112
774 Tsai PS, Blinder P, Migliori BJ, Neev J, Jin Y, Squier JA, Klenfeld D. 2009. Plasma-mediated ablation: An
775 optical tool for submicrometer surgery on neuronal and vascular systems. *Curr Opin Biotechnol*
776 **20**:90–99. doi:10.1007/s11103-011-9767-z.Plastid
777 Tschöp MH, Speakman JR, Arch JRS, Auwerx J, Brüning C, Chan L, Eckel RH, Jr RVF, Galgani JE, Hambly
778 C, Herman MA, Horvath TL, Kahn BB, Sara C. 2013. A guide to analysis of mouse energy
779 metabolism. *Nat Methods* **9**:57–63. doi:10.1038/nmeth.1806.A
780 Wang M, Kim M, Xia F, Xu C. 2019. Impact of the emission wavelengths on in vivo multiphoton
781 imaging of mouse brains. *Biomed Opt Express* **10**:1905–1918.
782 Wang M, Wu C, Sinefeld D, Li B, Xia F, Xu C. 2018. Comparing the effective attenuation lengths for
783 long wavelength in vivo imaging of the mouse brain. *Biomed Opt Express* **9**:3534.
784 doi:10.1364/BOE.9.003534
785 Wang T, Ouzounov DG, Wu C, Horton NG, Zhang B, Wu CH, Zhang Y, Schnitzer MJ, Xu C. 2018. Three-
786 photon imaging of mouse brain structure and function through the intact skull. *Nat Methods*
787 **15**:789–792. doi:10.1038/s41592-018-0115-y
788 Weisenburger S, Tejera F, Demas J, Chen B, Manley J, Sparks FT, Martínez Traub F, Daigle T, Zeng H,
789 Losonczy A, Vaziri A. 2019. Volumetric Ca2+ Imaging in the Mouse Brain Using Hybrid
790 Multiplexed Sculpted Light Microscopy. *Cell* 1–17. doi:10.1016/j.cell.2019.03.011
791 Wilt BA, Fitzgerald JE, Schnitzer MJ. 2013. Photon shot noise limits on optical detection of neuronal
792 spikes and estimation of spike timing. *Biophys J* **104**:51–62. doi:10.1016/j.bpj.2012.07.058
793 Xiong B, Li A, Lou Y, Chen S, Long B, Peng J, Yang Z, Xu T, Yang X, Li X, Jiang T, Luo Q, Gong H. 2017.
794 Precise Cerebral Vascular Atlas in Stereotaxic Coordinates of Whole Mouse Brain. *Front*
795 *Neuroanat* **11**:1–17. doi:10.3389/fnana.2017.00128
796 Xu C, Webb WW. 1997. Multiphoton Excitation of Molecular Fluorophores and Nonlinear Laser
797 MicroscopyTopics in Fluorescence Spectroscopy, Vol. 5. Springer. p. 473.
798 Yang W, Yuste R. 2017. In vivo imaging of neural activity. *Nat Methods* **14**:349–359.
799 doi:10.1038/nmeth.4230
800 Yildirim M, Sugihara H, So PTC, Sur M. 2019. Functional imaging of visual cortical layers and subplate
801 in awake mice with optimized three-photon microscopy. *Nat Commun* **10**. doi:10.1038/s41467-
802 018-08179-6
803

# Appendix 1

## Estimation of the Cross-over Depth Based on Fluorophore Cross Section

The number of signal photons generated per excitation pulse at the focus can be calculated according to equations (8) and (9), for 2PE and 3PE in a Gaussian beam focus respectively (Xu and Webb, 1997):

$$\text{2PE signal photons per pulse} = \frac{S_{2P}}{f} = \frac{1}{2}\frac{g_p^{(2)}}{\tau}\phi C(\eta\sigma_2)n_0\frac{\pi}{\lambda_{2P}}\left(\frac{P_{2P}}{f}\right)^2 \quad (8)$$

$$\text{3PE signal photons per pulse} = \frac{S_{3P}}{f} = \frac{1}{3}\frac{g_p^{(3)}}{\tau^2}\phi C(\eta\sigma_3)n_0\frac{2\pi^2}{3\lambda_{3P}^3}\text{NA}^2\left(\frac{P_{3P}}{f}\right)^3 \quad (9)$$

where $g_p^{(n)}$ is the nth-order temporal coherence factor (we assume a Gaussian temporal profile of the pulse); $\tau$ is the laser pulse width; $\phi$ is the system collection efficiency; $C$ is the concentration of the fluorophore; $\eta\sigma_n$ is the n-photon action cross section; $n_0$ is the refractive index of the medium; $\lambda$ is the excitation wavelength in vacuum; NA is the numerical aperture defined by $1/e^2$ beam diameter at the objective back aperture; $P_{2P}$ and $P_{3P}$ are, respectively, the average power at the focus for 2PE and 3PE in the unit of photons/s, and $f$ the repetition rate.

At a typical signal yield for three-photon imaging at 0.1 photons detected per excitation pulse (i.e. $S_{3P}/f = 0.1$), the required pulse energy at the focus (i.e. $\frac{P_{3P}}{f}\cdot\frac{hc}{\lambda_{3P}}$) has been measured to be ~2 nJ. For the 2PE signal yield to be the same as 3PE (i.e. $S_{2P}/f = 0.1$), the 2PE pulse energy at the focus can be derived from equations (8) and (9):

$$\frac{P_{2P}}{f} = \sqrt{\frac{4\pi}{9}\frac{1}{\tau}\frac{g_p^{(3)}}{g_p^{(2)}}\frac{\sigma_3}{\sigma_2}\frac{\lambda_{2P}}{\lambda_{3P}{}^3}\text{NA}^2\left(\frac{P_{3P}}{f}\right)^3} \quad (10)$$

For estimation, we use $10^{-49}$ cm$^4$ s/photons and $10^{-82}$ cm$^6$ (s/photons)$^2$ for 2PE and 3PE action cross sections, respectively, based on the typical values of fluorescent dyes and calcium indicators (Cheng et al., 2014; Macklin and Harris, 2016a, 2016b). Evaluating equation (10**)** with all the parameter values listed in Table S1, 2PE pulse energy (i.e. $\frac{P_{2P}}{f} \cdot \frac{hc}{\lambda_{2P}}$) is solved to be 0.2 nJ. In other words, the ratio of 3PE to 2PE pulse energy resulting in 0.1 photons detected per excitation pulse is 2 nJ/0.2 nJ = 10 times, close to the 8x measured with GCaMP6s (Figure 1B). The ratio measured with fluorescein is higher (15x) because fluorescein 3PE cross section at ~ 1320 nm is noticeably smaller than $10^{-82}$ cm$^6$ (s/photons)$^2$ and 1320 nm is likely not the peak 3PE wavelength for fluorescein (Macklin and Harris, 2016b).

**Table S1. Two- and three-photon Excitation Parameters.**

| | Objective Lens Focal Length (mm) | 1/e$^2$ Beam Diameter at the Back Aperture (mm) | Effective NA | Pulse Duration τ (fs) | $g_p^{(n)}$ |
|---|---|---|---|---|---|
| 920 nm 2PE | 7.2 | 11 | 0.75 | 60 | 0.66 |
| 1320 nm 3PE | 7.2 | 11 | 0.75 | 60 | 0.51 |

The cross-over depth is defined as the imaging depth where an equal amount of signal per pulse is generated using the same pulse energy at the brain surface for 1320-nm 3PE and 920-nm 2PE. Based on the ratio of 3PE to 2PE pulse energy and the EALs at 1320 nm and 920 nm, the cross-over depth can be readily calculated by solving for z in equation (11):

$$\frac{\text{3PE pulse energy at the focus}}{\text{2PE pulse energy at the focus}} = \frac{\text{surface 3PE pulse energy} \times \exp\left[-\mathrm{z}/l_e(1320\mathrm{nm})\right]}{\text{surface 2PE pulse energy} \times \exp\left[-\mathrm{z}/l_e(920\mathrm{nm})\right]} \qquad (11)$$

For example, with $l_e$ (1320nm) = 293 µm, and $l_e$ (920nm) = 154 µm (Figure 1B), and the pulse energy ratio of 8 for GCaMP6s, the cross-over depth z is solved to be 675 µm. If the pulse energy ratio of 15 for fluorescein is used, the cross-over happens at 880 µm.

The ratio of 3PE to 2PE pulse energy can also be used to calculate the 3PE cross section based on the known 2PE cross section of the same fluorescent molecule. From Eq. (12), the ratio of 3PE to 2PE cross section can be expressed as:

$$\frac{\sigma_3}{\sigma_2} = \frac{9}{4\pi}\tau\frac{g_p^{(2)}}{g_p^{(3)}}\frac{(\lambda_{3\mathrm{P}})^3}{\lambda_{2\mathrm{P}}}\frac{1}{\mathrm{NA}^2}\left(\frac{P_{2P}}{P_{3P}}\right)^2\left(\frac{P_{3P}}{f}\right)^{-1} \quad (12)$$

Eq. (12) shows the advantage of such a ratiometric measurement since there is no need to estimate the intracellular dye concentration $C$ or system collection efficiency $\phi$. Given the measured 2PE action cross section of GCaMP6s around 920 nm (~$2\times10^{-49}$ $cm^4s$ with saturated $Ca^{2+}$) (Dana et al., 2016), 3PE action cross section of GCaMP6s at 1320 nm is estimated to be ~$3\times10^{-82}$ $cm^6s^2$. This result is close to the 3PE action cross section of GCaMP6f measured in an independent study ($1.9\times10^{-82}$ $cm^6s^2$ with saturated $Ca^{2+}$) (Macklin and Harris, 2016b).